Collisionless Shocks Driven by Supersonic Plasma Flows with Self-Generated Magnetic Fields

C. K. Li,[1,*] V. T. Tikhonchuk,[2,3,†] Q. Moreno,[2,3] H. Sio,[1] E. D'Humières,[2] X. Ribeyre,[2] Ph. Korneev,[4,5] S. Atzeni,[6]
R. Betti,[7] A. Birkel,[1] E. M. Campbell,[7] R. K. Follett,[7] J. A. Frenje,[1] S. X. Hu,[7] M. Koenig,[8] Y. Sakawa,[9]
T. C. Sangster,[7] F. H. Seguin,[1] H. Takabe,[9] S. Zhang,[10] and R. D. Petrasso[1]

[1]*Plasma Science and Fusion Center, Massachusetts Institute of Technology, Cambridge, Massachusetts 02139, USA*
[2]*Centre Lasers Intenses et Applications, University of Bordeaux, CNRS, CEA, 33405 Talence, France*
[3]*ELI-Beamlines, Institute of Physics, Czech Academy of Sciences, 25241 Dolní Břežany, Czech Republic*
[4]*National Research Nuclear University MEPhI, 115409 Moscow, Russian Federation*
[5]*P. N. Lebedev Physics Institute, Russian Academy of Sciences, 119991 Moscow, Russian Federation*
[6]*Dipartimento SBAI, Università di Roma "La Sapienza," I-00161 Roma, Italy*
[7]*Laboratory for Laser Energetics, University of Rochester, Rochester, New York 14627, USA*
[8]*Laboratorire pour l'Utilisation de Lasers Intenses, CNRS CEA, Université Paris VI,
École Polytechnique, 91128 Palaiseau, France*
[9]*Institute of Laser Engineering, Osaka University, Osaka 565-0871, Japan*
[10]*University of California San Diego, La Jolla, California 92093, USA*

Collisionless shocks are ubiquitous in the Universe as a consequence of supersonic plasma flows sweeping through interstellar and intergalactic media. These shocks are the cause of many observed astrophysical phenomena, but details of shock structure and behavior remain controversial because of the lack of ways to study them experimentally. Laboratory experiments reported here, with astrophysically relevant plasma parameters, demonstrate for the first time the formation of a quasiperpendicular magnetized collisionless shock. In the upstream it is fringed by a filamented turbulent region, a rudiment for a secondary Weibel-driven shock. This turbulent structure is found responsible for electron acceleration to energies exceeding the average energy by two orders of magnitude.

The generation of electromagnetic collisionless shocks [1–3] in the laboratory is an important goal for elucidating large-scale astrophysical phenomena, supernova remnants, protostellar jets, accreting compact objects [4–7], and studying a broad range of fundamental physics phenomena [3,7–21]. The broadband, nonthermal emissions observed in various astrophysical objects have been attributed to synchrotron and inverse Compton radiation emitted by electrons accelerated through interactions with magnetic irregularities across the shock fronts via the first-order Fermi mechanism [3–5].

Shocks in astrophysics often have a high ratio of the thermal plasma pressure to magnetic field pressure (β), low collisionality, and are supercritical and super Alfvénic [3,14]. Such shocks may be mediated by magnetic turbulence spontaneously generated by plasma instabilities. Magnetic fluctuations scatter and reflect incoming particles out of the thermal pool from the shock ramp to the upstream, providing essential mechanisms for energy dissipation and particle acceleration. The electromagnetic ion Weibel instability [22] excited in counterpropagating plasma streams is considered as being one of the mechanisms responsible for these collective processes. It grows

fast and results in current filaments and magnetic turbulence [7–10].

Laboratory experiments that have the critical shock properties of astrophysical regimes [14] are extremely difficult due to the temporal and spatial scales available with present facilities. In most previous experiments, the plasmas had to meet strict conditions: $\lambda_{\rm mfp} \gg \ell_{\rm int} \gg \ell_{\rm EM}$, where $\lambda_{\rm mfp}$ is the ion-ion mean free path, $\ell_{\rm int}$ is the characteristic size of interaction region, $\ell_{\rm EM} = Kc/\omega_{\rm pi}$ is the scale for instability growth, and $c/\omega_{\rm pi} = (m_i/\mu_0 Z^2 e^2 n_i)^{1/2}$ is the ion skin depth. Here, m_i and Ze are the ion mass and charge, K is a numerical factor depending on the process of shock formation, and μ_0 is the vacuum magnetic permittivity. Numerical simulations have shown that in the nonrelativistic regime, a large value of $K(\gtrsim 100)$ is required for generating these shocks [8]. As the realization of these conditions requires a large plasma volume and a large driver energy [8,14], laboratory experiments resulted in the Weibel instability in counterstreaming plasma flows but without generating collisionless shocks [16,17].

Magnetization of electrons in upstream plasma has been shown to drastically change the conditions for collisionless shock formation through compressing the preexisting
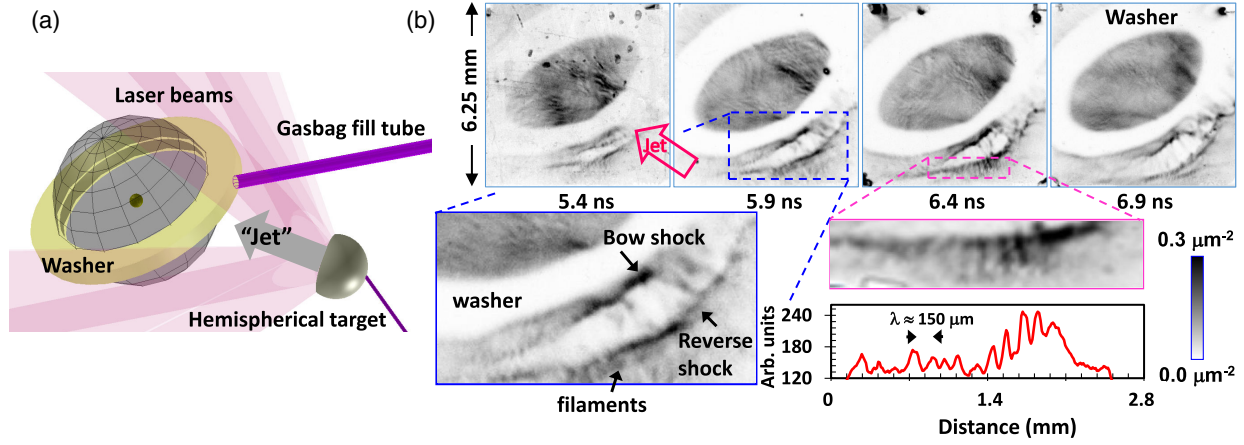
FIG. 1. (a) Side-on view of the experiment from the proton imager, which is 15 cm from the target chamber center (TCC). The proton backlighter is 1 cm from the TCC, opposing the imager [25]. (b) Side-on radiographs (in target plane) sampled at four different times with 3.3-MeV protons. Arrow at the right-lower corner of the image at $t = 5.4$ ns points in the direction of jet propagation. Crescent-shaped, quasiperpendicular magnetized shocks are formed in front of the washer. Enlarged structure of the shocks and filaments at $t = 5.9$ and 6.4 ns.

magnetic field and forming a pistonlike structure [18,19]. But the shocks reported in these articles were not accompanied by upstream plasma turbulence and thus cannot provide a multipass particle acceleration, which is the main interest for high energy astrophysics. We performed an experiment that, for the first time, demonstrated the formation of an electromagnetic collisionless shock with magnetic turbulence, and electron energization. Our experiment revealed a novel physical scenario of a fast collisionless shock formation ($K \sim 2$–3) with Weibel-driven plasma turbulence and magnetic field compression. We showed that the shock formation can proceed quickly on a small spatial scale when electrons are magnetized in the upstream plasma. In a difference from previous studies, we have an asymmetric configuration with one plasma carrying magnetized electrons and another one without magnetic field. Consequently, the interaction region contains two different zones: a Weibel unstable one and a compressed one.

The experiments were conducted at the OMEGA Laser Facility [23] with a configuration illustrated in Fig. 1(a). A collimated plasma jet was generated by six laser beams, each with an energy 500 ± 10 J and duration of 1 ns, arriving simultaneously with uncertainty ± 25 ps. These beams were focused symmetrically to focal spots of 820 μm in diameter in the interior of a plastic hemispherical target. This target had a diameter of 1.8 mm and was placed at 7 mm from the target chamber center. The plasma jet, propagating with a velocity $u_{jet} \gtrsim 1200$–1400 km s^{-1} [24] and electron density $n_e \sim 5 \times 10^{18}$ cm^{-3}, interacted with a polyimide-shell gasbag filled with a 0.1-bar hydrogen gas. The experiments were diagnosed with four complementary techniques: (i) Thomson scattering from 4th-harmonic laser light, was used for measuring the density, temperature, and velocity of the jet. This probing beam was the OMEGA beam No. 25, directed to the TCC

in separate shots without the gasbag; (ii) monoenergetic 3.3- and 15-MeV protons (from DD and D^3He fusion reactions), for radiographing the magnetic fields [25]; (iii) plasma self-emission in the soft x-ray range for imaging the plasma density distribution; and (iv) electron spectroscopy, for measuring the energy distribution of electrons escaping the plasma. The experiment was simulated and modeled with a two-dimensional (2D) radiation hydrodynamic code FLASH [26] (for laser-plasma interaction and jet formation), and with a 2D kinetic particle-in-cell (PIC) code PICLS [27] (for jet-gasbag interaction and shock formation).

The first stage of the experiment is a high-velocity jet interaction with the gasbag. Jet ions deposit their kinetic energy (~ 7–10 keV/nucleon) in the shell, since their range (~ 1 μm [28]) is comparable with the 0.8-μm shell thickness. The energy (~ 10 MJ/g) deposited in the shell induces its explosion with a velocity $u_{shell} \cong 300$–400 km/s. Interaction of the expanding shell material with the jet is the origin of the structure shown in Fig. 1(b). Four time-gated, side-on proton radiographs with spatial resolution ~ 40 μm [25] show filaments aligned radially with the shell expansion and the moving crescent-shaped, dark transverse features, identified as the fronts of the bow (forward) and reverse shocks. Details of this double shock structure, enlarged from a radiograph at $t = 5.9$ ns, show that both shocks have a typical width of a few hundred microns. The bow shock decelerates the expanding shell plasma and the reverse shock decelerates the jet plasma. The filaments, with a measured period of ~ 150 μm, are more pronounced at later times, as shown in the enlarged image at $t = 6.4$ ns. The reverse shock velocity $u_{shock} \cong 600$–300 km s^{-1} was measured from the time evolution of the distance between the shock front and washer edge. The forward bow shock remains approximately at the same position during the observation.
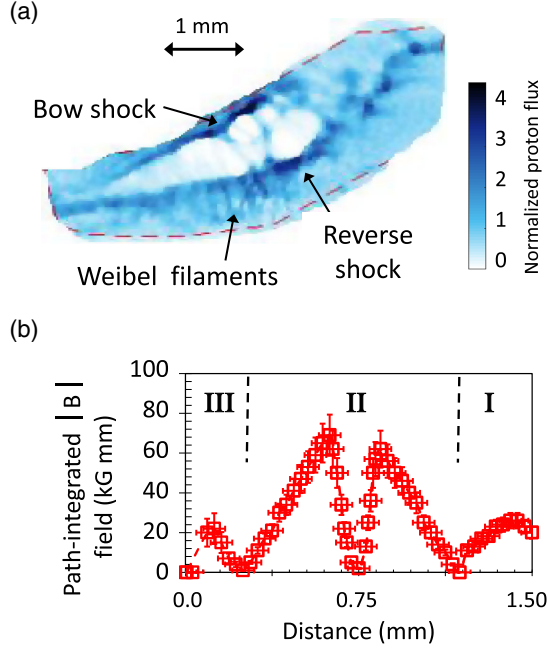
FIG. 2. (a) 2D reconstruction of proton radiograph at $t = 6.4$ ns (on the target plane) showing the shocks and filaments. (b) Diagonal lineout across the shocked region (transversely averaged over 1 mm width) gives the strength of the magnetic fields.

The structure of path-integrated magnetic fields was reconstructed from experimental data [29]. The contribution of electric fields to proton beam deflection is shown to be negligible by comparing proton radiographs taken from the opposite sides of the interaction zone. The spatial topology of the reconstructed magnetic fields shows three different regions: (I) from the reverse shock front to upstream; (II) the shocked region consisting of compressed jet and expanding shell plasma; and (III) upstream the expanding shell. The ratio of the parallel to the perpendicular field component is 0.1 ≪ 1, so the observed shocks are quasiperpendicular. The consistency of the magnetic field analysis is proved by the simulated proton radiograph in Fig. 2(a), which is based on the reconstructed magnetic field. A lineout across the double shocks gives a distance ∼1 mm between the shock fronts, and shock widths ∼200–300 μm, which are 2–3 times larger than the ion skin depth.

The magnetic fields observed in upstream zone III are a factor of 3 smaller than the peak strength in the shocked region [Fig. 2(b)]. We attribute the source of the upstream magnetic fields in zone III to be the Biermann battery effect [30,31]. Hydrodynamic simulations indicate that such fields are generated in the expanding shell plasma. The strength of these magnetic fields is about 20–30 kG, consistent with the path-integrated magnetic field in region III assuming the backlighting proton path length in plasma $\ell \sim 1$ mm. Figure 2(b) shows the field strength jump in region II from regions III, i.e., $B_{\text{II}}/B_{\text{III}} \sim 3$. In contrast,

there is no regular magnetic field in region I, but there is a Weibel-generated magnetic field with a similar amplitude, varying on a scale of 150 μm. A threefold increase of field strength across the bow shock front provides experimental evidence of enhancement of the Biermann fields in the overlapping region. This magnetic field compression is the key to fast shock formation.

The plasma density distribution across the shock is evaluated independently by measuring the bremsstrahlung x-ray emission from the interaction zone. A relatively minor electron temperature contribution to the intensity of bremsstrahlung emission ($\propto Z_{\text{eff}}^3 n_i^2 \sqrt{T_e}$) relates the measured x-ray fluence change across the shock front to the plasma density jump. From Fig. 3, considering an effective ion charge $Z_{\text{eff}} \sim 2$ which corresponds to the electron temperature ∼50 eV measured by Thomson scattering, we infer the density jump to be $\rho_{\text{II}}/\rho_{\text{I}} \sim 3$, which agrees qualitatively with the magnetic field jump. Assuming similar upstream plasma densities, $\rho_{\text{I}} \sim \rho_{\text{III}}$, one can apply the Rankine-Hugoniot conditions for a quasiperpendicular shock in a weak magnetic field [32]

$$\frac{B_{\text{II}}}{B_{\text{III}}} \approx \frac{\rho_{\text{II}}}{\rho_{\text{III}}} \approx \frac{(\gamma + 1)M^2}{2 + (\gamma - 1)M^2} \sim 3,$$

and evaluate the shock Mach number in the shock frame, $M = u_{\text{shock}}/c_s \approx 3$, for the adiabatic index $\gamma \approx 5/3$. The upstream acoustic velocity $c_s \approx 100$ km/s is evaluated from the upstream temperature $T_e \approx 50$–100 eV, measured with Thomson scattering, and calculated with a hydrodynamic code.

According to Fig. 1, the bow shock doesn't move in the laboratory frame. Assuming the expanding shell velocity $u_{\text{shell}} \cong 300$ km s^{-1}, a Mach number of 3 leads to the plasma flow velocity in zone II $u_{\text{II}} \cong 100$ km s^{-1}, corresponding to -300 km s^{-1} in the reverse shock reference frame. The reverse shock velocity in the laboratory frame, $u_{\text{shock}} \approx 400$ km s^{-1}, was measured by proton radiography. Assuming the Mach number of the reverse shock to be 3, this gives rise to a normal component of jet velocity $u_{\text{I}} \sim 500$ km s^{-1}, a reasonable value as the shocks are generated at the flanks of the expanding shell [Fig. 1(b)]. Knowing the upstream plasma density $n_e \approx 5 \times 10^{18}$ cm^{-3} from Thomson scattering, we estimate the pressure ratio in the upstream plasma $\beta = 2\mu_0 n_e T_e/B^2 \approx 20$, which leads to a ratio of acoustic to Alfvén velocity $c_s/c_A = \sqrt{\beta} \approx 4.5$. Consequently, the shock is super Alfvénic with $M_A = u_{\text{shock}}/c_A \approx 14$.

Shock formation and particle acceleration have previously been studied for various astrophysical and laboratory conditions in many PIC simulations [8–10,31,33–37]. They do not, however, fully reproduce our experimental conditions for which the expanding shell plasma carrying self-generated magnetic field interacts with a fast-moving plasma jet. To explore this in detail, the shock formation
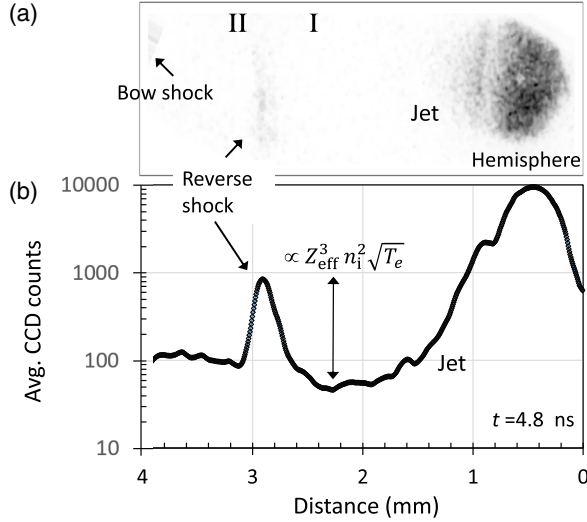
FIG. 3. (a) Side-on x-ray self-emission image shows the laser-driven hemisphere, plasma jet (propagates from the right to left), and reverse shock (travels from the left to right). The bow shock can be seen in the upper left image, which is about 1 mm away from the reverse shock, consistent with Figs. 1 and 2. (b) The lineout along jet propagation provides relative emissions from the different objects (±20%).

was modeled with a PIC simulation in the jet frame with a reduced ion-to-electron mass ratio of $m_i/m_e = 200$ and without collisions. The simulation box size was $600\,c\omega_{pe}^{-1}$ in both directions with a resolution of $0.5\,c\omega_{pe}^{-1}$, 50 particles per cell, and absorbing boundaries. The expanding plasma carries a homogeneous magnetic field $B_0 = 20$ kG, has an ion density $n_i = 10^{18}$ cm^{-3} and temperature $T_1 = 100$ eV, propagates at velocity $u_i = 2000$ km s^{-1}, and interacts with an unmagnetized plasma of the same density but with temperature $T_2 = 10$ eV at $x > 0$. Shown in Figs. 4(a) and 4(c) are the late stages of interaction at $t \sim 2000\,\omega_{pi}^{-1}$, where the magnetic field (a), and plasma density (c) are compressed to a factor of $\lesssim 3$. The shock front shown in Figs. 4(b) and 4(d) moves at one third of the

ion flow velocity, which is consistent with the observations. The Weibel instability is observed upstream the magnetized zone due to the penetration of ions. The Weibel filaments, generating magnetic turbulence, transfer ion energy to the electrons. Simulation indicates an electron temperature increase to 2 keV in the magnetized region after the shock formation, a signature of significant particle heating and entropy dissipation due to magnetic turbulence. The quantitative agreement between the 2D PIC simulation and the experiments demonstrates the robustness of the considered process of shock formation from the magnetic piston. This process is not much affected by the reduction of the third dimension. However, the nonlinear stage of the Weibel instability observed in the experiments requires a special 3D analysis for further understanding of the upstream magnetic turbulence and electron acceleration.

Detailed analysis of the PIC simulation shows a two-step process of shock formation. First, the Biermann magnetic field is compressed in the interaction region. This is explained by increased electron density and conservation of magnetic flux. The magnetized zone extends at a speed twice slower than the ion speed, and has a density equal to the sum of densities of the jet and shell plasmas. Eventually, the width of this structure becomes comparable to the ion Larmor radius, and it transforms into a shock. When the magnetic field jump is accompanied by the jumps of ion density and ion flow velocity according to the Rankine-Hugoniot conditions, a shock is formed.

The ion Weibel instability is excited upstream in the magnetic field compression zone, where the jet ions overlap with the shell plasma ions. It is maintained after the shock formation by ions reflected upstream from the shock front. Although the Weibel instability is not needed for the shock formation [18,19], it facilitates that process. Eventually, it will form a secondary shock in the upstream region [8–10] on a much longer timescale. In addition, it provides conditions for a multipass electron stochastic acceleration. The experimental evidence for that process is presented in Fig. 5(a), which shows the electron energy distributions
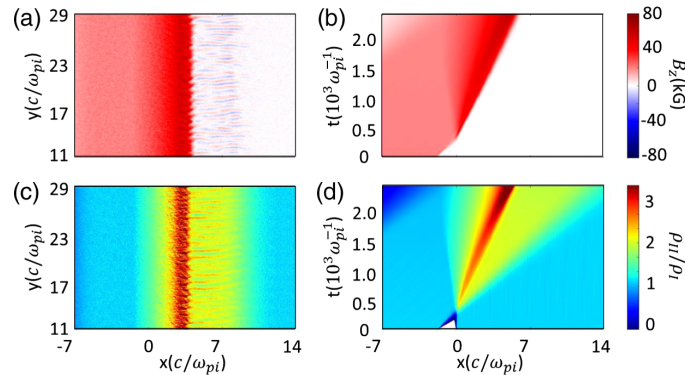

FIG. 4. 2D PIC simulations of two counterstreaming plasmas. Left column shows distribution of the magnetic field (a) and ion density (c) at the end of simulation ($t \sim 2000\,\omega_{pi}^{-1}$). Right column shows temporal evolution of the magnetic field (b) and density (d) averaged over the transverse coordinate (y).
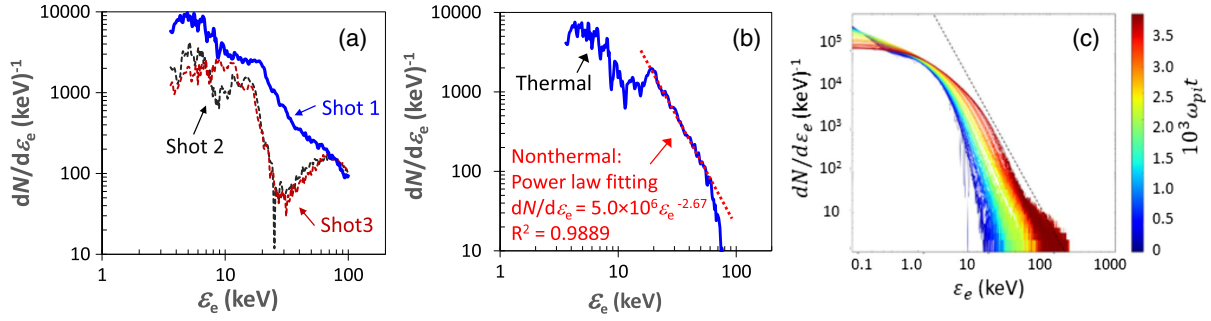
FIG. 5.   (a) Electron spectra measured at a direction perpendicular to the jet propagation with (shot 1) and without (shots 2 and 3) gasbags. (Error in electron number $\pm 28\%$ [38]; error in electron energy $\pm 20\%$.) (b) The electron spectrum shows a structure of two components: thermal and nonthermal. (c) Simulated temporal evolution of the electron energy distribution. The electron energy is multiplied by 10, because the electron mass was 10 times larger than the real electron mass. The color code shows the temporal evolution.

measured with and without gasbags. A significant difference can be seen in the electron energy ranges $\varepsilon_e \sim$ 3–10 keV and 15–60 keV. After subtracting the backgrounds, the electron spectrum in Fig. 5(b) shows two components—a thermal part and a nonthermal tail. The thermal part, with a temperature $T_e \sim 2$ keV, agrees with the calculated electron temperature downstream the shock. The nonthermal part contains $\sim 20\%$ of the total electron population with a factor of 10–60 higher energies. These results are reproduced in the PIC simulation [Fig. 5(c)].

The observed energetic electrons indicate an efficient multipass acceleration. Assuming the size of the turbulence region upstream the shock to be 1 mm, an electron with an energy of a few keV may cross it more than 10 times and gain energy in subsequent collisions with the shock and with the turbulence. At present it is difficult to make a clear distinction between the mechanisms of diffusive [4,5] and drift [39] acceleration, but we exclude the whistler and low hybrid wave turbulence [40] as there is no regular magnetic field upstream of the shock. In contrast, the measured spectrum is consistent with the idea of a multipass, first-order Fermi acceleration operating in the shock and assisted by the upstream Weibel turbulence. It is quantitatively justified by a power-law spectrum of the non-thermal component in the energy range 15–60 keV [see Figs. 5(b) and 5(c)]. The measured distribution $dN/d\varepsilon_e \propto \varepsilon_e^{-2.67}$ is consistent with first-order Fermi acceleration [4,5]: $dN/d\varepsilon_e \propto \varepsilon_e^{-\mu}$, where $\mu = (r+2)/(r-1)$. For the estimated shock compression, $r = \rho_{\text{II}}/\rho_{\text{I}} = 3$, the expected slope is $\mu = 2.5$; this compares with $\mu \approx 3$ obtained in the simulation; the difference is explained by a short shock lifetime.

The reported experimental conditions are relevant to collisionless shocks in astrophysical regimes. The mean free path of carbon ions with a velocity $u_i = 1000$ km s^{-1} relative to a plasma with ion density $n_i \approx 10^{18}$ cm^{-3} is estimated [15] to be $\lambda_{\text{mfp}} \gtrsim 1$ cm, which is much greater than the observed shock width of 200–300 μm. The ion collision frequency is much less than the ion cyclotron frequency ($\nu_{\text{ii}} \sim 2 \times 10^8/\text{s} \ll \omega_{\text{ci}} \sim 10^9/\text{s}$), indicating that the measured shocks are essentially collisionless and magnetized. The inferred energy density of magnetic fields is at the level $\sigma \sim 1\%$ of equipartition ($\sigma = B^2/\mu_0 \rho u_{\text{shock}}^2$), which is a typical value for SNR and GRB afterglows [6–8]. The large plasma $\beta \sim 20$ and large values of the acoustic and Alfvén Mach numbers, $M \sim 3$ and $M_A \sim 14$, respectively, as well as small magnetization ($\sim 1/M_A^2$), indicate that the measured shocks are supercritical and super Alfvénic. The observed power-law spectrum reaffirms the formation of an electromagnetic collisionless shock in this experiment.

In summary, we have generated in the laboratory a high-Alfvénic-Mach-number, nonrelativistic, possibly astrophysically relevant, electromagnetic collisionless shock accompanied by Weibel-driven magnetic turbulence. This work advances our knowledge of collisionless shocks in nonrelativistic regimes, and demonstrates that laser-matter interactions offer a powerful platform for exploring collisionless shocks in a broader context.

*ckli@mit.edu

†vladimir.tikhontchouk@u-bordeaux.fr

[1] R. McCray and T. P. Snow, Jr., Annu. Rev. Astron. Astrophys. **17,** 213 (1979).

[2] C. P. McKee and D. J. Hollenbach, Annu. Rev. Astron. Astrophys. **18,** 219 (1980).

[3] R. Treumann, Astron. Astrophys. Rev. **17,** 409 (2009).

[4] A. R. Bell, Mon. Not. R. Astron. Soc. **182,** 147 (1978).

[5] R. Blanford and D. Eichler, Phys. Rep. **154,** 1 (1987).

[6] K. Koyama, R. Petre, E. V. Gotthelf, U. Hwang, M. Matsuura, M. Ozaki, and S. S. Holt, Nature (London) **378,** 255 (1995).

[7] M. V. Medvedev and A. Loeb, Astrophys. J. **526,** 697 (1999).

[8] T. Kato and H. Takabe, Astrophys. J. **681,** L93 (2008).

[9] L. Q. Silva, R. A. Fonseca, J. W. Tonge, J. M. Dawson, W. B. Mori, and M. V. Medvedev, Astrophys. J. Lett. **596,** L121 (2003).

[10] A. Spitkovsky, Astrophys. J. Lett. **673,** L39 (2008).

[11] J. T. Frederiksen, C. B. Hededal, T. Haugbølle, and Å. Nordlund, Astrophys. J. **608,** L13 (2004).

[12] B. A. Remington et al., Science **284,** 1488 (1999).

[13] G. Gregori, B. Reville, and F. Miniati, Phys. Rep. **601,** 1 (2015).

[14] R. P. Drake, Phys. Plasmas **7,** 4690 (2000).

[15] H. S. Park et al., High Energy Density Phys. **8,** 38 (2012).

[16] W. Fox, G. Fiksel, A. Bhattacharjee, P.-Y. Chang, K. Germaschewski, S. X. Hu, and P. M. Nilson, Phys. Rev. Lett. **111,** 225002 (2013).

[17] C. M. Huntington et al., Nat. Phys. **11,** 173 (2015).

[18] C. Niemann et al., Geophys. Res. Lett. **41,** 7413 (2014).

[19] D. B. Schaeffer, W. Fox, D. Haberberger, G. Fiksel, A. Bhattacharjee, D. H. Barnak, S. X. Hu, and K. Germaschewski, Phys. Rev. Lett. **119,** 025001 (2017).

[20] L. Romagnani et al., Phys. Rev. Lett. **101,** 025004 (2008).

[21] Y. Kuramitsu et al., Phys. Rev. Lett. **106,** 175002 (2011).

[22] E. B. Weibel, Phys. Rev. Lett. **2,** 83 (1959).

[23] J. M. Soures et al., Phys. Plasmas **3,** 2108 (1996).

[24] C. K. Li et al., Nat. Commun. **7,** 13801 (2016).

[25] C. K. Li et al., Phys. Rev. Lett. **97,** 135003 (2006).

[26] P. Tzeferacos, M. Fatenejad, N. Flocke, C. Graziani, G. Gregori, D. Q. Lamb, D. Lee, J. Meinecke, A. Scopatz, and K. Weide, High Energy Density Phys. **17,** 24 (2015).

[27] Y. Sentoku and A. J. Kemp, J. Comput. Phys. **227,** 6846 (2008).

[28] J. F. Ziegler et al., SRIM—The Stopping and Range of Ions in Matter (Ion Implantation Press, 2008).

[29] A. F. A. Bott, C. Graziani, P. Tzeferacos, T. G. White, D. Q. Lamb, G. Gregori, and A. A. Schekochihin, J. Plasma Phys. **83,** 905830614 (2017).

[30] L. Biermann, Z. Naturforsch **5A,** 65 (1950).

[31] T. Umeda et al., Phys. Plasmas **26,** 032303 (2019).

[32] R. Fitzpatrick, Plasma Physics: An Introduction, 1st ed. (CRC Press;Taylor & Francis Group, Boca Raton, FL, 2015).

[33] X. Guo, L. Sironi, and R. Narayan, Astrophys. J. **794,** 153 (2014).

[34] A. Grassi, M. Grech, F. Amiranoff, A. Macchi, and C. Riconda, Phys. Rev. E **96,** 033204 (2017).

[35] W. Fox, J. Matteucci, C. Moissard, D. B. Schaeffer, A. Bhattacharjee, K. Germaschewski, and S. X. Hu, Phys. Plasmas **25,** 102106 (2018).

[36] C. Ruyer, L. Gremillet, A. Debayle, and G. Bonnaud, Phys. Plasmas **22,** 032102 (2015).

[37] F. Fiuza, R. A. Fonseca, J. Tonge, W. B. Mori, and L. O. Silva, Phys. Rev. Lett. **108,** 235004 (2012).

[38] T. Bonnet, M. Comet, D. Denis-Petit, F. Gobet, F. Hannachi, M. Tarisien, M. Versteegen, and M. M. Aléonard, Rev. Sci. Instrum. **84,** 103510 (2013).

[39] L. Ball and D. Melrose, Pub. Astron. Soc. Aust. **18,** 361 (2001).

[40] A. Rigby et al., Nat. Phys. **14,** 475 (2018).